XAS and DFT Investigation of Mononuclear Cobalt(III)-Peroxo Complexes: Electronic Control of Geometric Structure in CoO$_2$ versus NiO$_2$ Systems

Ritimukta Sarangi[1], **Jaeheung Cho**[2], **Wonwoo Nam**[2], and **Edward I. Solomon**[1,3]

Ritimukta Sarangi: ritis@slac.stanford.edu; Edward I. Solomon: edward.solomon@stanford.edu

[1]Stanford Synchrotron Radiation Laboratory, SLAC National Accelerator Laboratory, Menlo Park, CA 94025, USA

[2]Department of Chemistry and Nano Science, Department of Bioinspired Science, Center for Biomimetic Systems, Ewha Womans University, Seoul 120-750, Korea

[3]Department of Chemistry, Stanford University, Stanford, CA 94305, USA

Abstract

The geometric and electronic structures of two mononuclear [(L)CoO$_2$]$^+$ complexes, [(12-TMC)CoO$_2$](ClO$_4$) (**1**) and [(14-TMC)CoO$_2$](ClO$_4$) (**2**), have been evaluated using Co K-edge x-ray absorption spectroscopy (XAS) and extended x-ray absorption fine structure (EXAFS) and correlated with density functional theory (DFT) calculations to evaluate the differences in geometric and electronic structure due to changes in the TMC chelate ring size. Co K-edge XAS shows that both **1** and **2** are Co(III) species. Co K-edge EXAFS data show that both **1** and **2** are side-on O$_2$ bound Co(III)-peroxide complexes. A combination of EXAFS and DFT calculations reveal that while the constrained 12-TMC ring in **1** allows for side-on O$_2$ binding to the Co center with ease, the 14-TMC chelate in **2** has to undergo significant distortion of the ring to overcome steric hindrance posed by the four *cis*-methyl groups of the chelate to allow side-on O$_2$ binding to the Co center. The Ni analogue of **2**, [(14-TMC)NiO$_2$]$^+$, has been shown to form an end-on bound Ni(II)-superoxide species. The electronic and geometric factors that determine the different electronic structures of **2** and [(14-TMC)NiO$_2$]$^+$ are evaluated using DFT calculations. The results show that while the sterics of the *cis*-14-TMC chelate contribute to the geometry of O$_2$ binding and results in an end-on bound Ni(II)-O$_2^-$ complex in [(14-TMC)NiO$_2$]$^+$, the higher thermodynamic driving force for the oxidation of the Co(II) overcomes this steric constraint, resulting in the stabilization of a side-on bound Co(III)-O$_2^{2-}$ electronic structure in **2**.

1. Introduction

Transition metal active sites of proteins play vital roles in dioxygen binding and reduction in a variety of important biological processes as they facilitate the spin-forbidden interaction between dioxygen and organic matter.[1-4] Understanding the mechanism of dioxygen binding and the geometric and electronic structures of the various intermediates generated in the process of dioxygen activation are of key importance in understanding the overall reaction mechanism of metalloproteins. In the case of mononuclear dioxygen activating

proteins, the first step involves the formation of a M-O$_2$ (M = metal active site) intermediate, which can either react directly or lead to the formation of a high-valent metal-oxo intermediate. This M-O$_2$ intermediate can potentially assume different O$_2$ binding modes (side-on or end-on), different oxidation states (O$_2$, O$_2^-$ or O$_2^{2-}$), different spin states at the metal center and different exchange stabilizations between the dioxygen moiety and the metal center. Biomimetic efforts have resulted in the synthesis of various M-O$_2$ (M-O) intermediates,[5-8] and spectroscopic characterization of these intermediates has been directed towards understanding factors that determine their electronic structure, which can make a key contribution to the reactivity.

Macrocyclic tetradentate N$_4$ ligands, such as 1,4,8,11-tetramethyl-1,4,8,11-tetraazacyclotetradecane (14-TMC), have been effectively used in synthesizing mononuclear metal-oxygen complexes (M = Cr, Mn, Fe and Ni).[9-13] Recently, we have successfully synthesized Ni-O$_2$ complexes with a variety of different TMC ligands[9,11] in which the ligand is varied from a 12-membered to a 14-membered ring (i.e., 12-TMC to 14-TMC; 12-TMC = 1,4,7,10-tetramethyl-1,4,7,10-tetraazacyclododecane). X-ray absorption spectroscopic (XAS) studies and density functional theory (DFT) calculations on [(12-TMC)NiO$_2$] and [(14-TMC)NiO$_2$] have revealed differences in electronic and geometric structures that are associated with large steric hindrance posed by the 14-TMC ring bound to the Ni center with all four methyl groups *cis* to the O$_2$ binding side (Scheme 1). These differences translate to reactivity differences; while [(12-TMC)NiO$_2$] (side-on bound Ni^{III}-O$_2^{2-}$) participates in nucleophilic reactions (aldehyde oxidation), [(14-TMC)NiO$_2$] (end-on bound Ni^{II}-O$_2^-$) is capable of conducting electrophilic oxidative reactions.[11]

LCo-O$_2$ complexes are important analogues of biological dioxygen carriers and have been synthesized with porphyrin, salen and N$_4$ macrocyclic ligands.[14-16] We have extended these synthetic efforts towards cobalt complexes to characterize reactivity differences of the (TMC)Co-O$_2$ complexes with changing macrocycle ring size.[17] In a recent crystal structure of [(12-TMC)CoO$_2$] (**1**), we have shown a side-on binding mode of the O$_2$ moiety to the Co center (Scheme 1) and showed that **1** is EPR silent. Resonance Raman (rR) data revealed an O-O stretching frequency of 902 cm^{-1} and Evan's method analysis of the NMR data show that **1** has no unpaired electrons. Together, these data indicate a ground state that is consistent with a S$_{total}$=0, Co(III)-O$_2^{2-}$ assignment of **1**. [(14-TMC)CoO$_2$] (**2**) has also been synthesized, while no crystal structure or rR data have been accessible, Evans method analysis of the NMR data revealed the presence of unpaired spin on the Co center.

In this study, the differences in electronic and geometric structure between **1** and **2** have been investigated using a combination of Co K-edge XAS, extended x-ray absorption fine structure (EXAFS) and DFT calculations. The factors that lead to the differences in magnetic properties of the two complexes have been evaluated. The role of the macrocyclic ligands in determining the geometric and electronic structure of the Co complexes is evaluated and compared and contrasted to its effects on the (TMC)Ni-O$_2$ complexes. These studies reveal interplay of contributions from steric effects, bonding interaction and the preferential stability of different oxidation states in determining the final electronic and geometric structures.

2. Experimental Section

2.1 Sample Preparation

[Co(12-TMC)O$_2$](ClO$_4$) (**1**),[17] [Co(14-TMC)O$_2$](ClO$_4$) (**2**),[18] [Co(12-TMC)(CH$_3$CN)] (ClO$_4$)$_2$ (**1$_{pre}$**, precursor of **1**)[17] and [Co(14-TMC)(CH$_3$CN)](ClO$_4$)$_2$ (**2$_{pre}$**, precursor of **2**)[18] were synthesized as previously described. ***Caution: Perchlorate salts are potentially explosive and should be handled with care!*** Since both **1** and **2** are thermally unstable, care

was taken to minimize decomposition during loading of the samples into the XAS cells and loading time was minimized. 2 mm lucite XAS cells were used with 37 μm Kapton windows for the solution samples of **1** and **2**. The solid samples for **1$_{pre}$** and **2$_{pre}$** were finely ground with BN into a homogeneous mixture and pressed into a 1 mm aluminum spacer between 37 μm Kapton windows. The samples were immediately frozen and stored under liquid N_2 conditions. During data collection, the samples were maintained at a constant temperature of $\sim$10 K using an Oxford Instruments CF 1208 liquid helium cryostat.

2.2 X-ray Absorption Spectroscopy

Co K-edge XAS data were measured on the frozen samples of both the oxygenated complexes, **1** and **2**, and their Co(II) precursors, **1$_{pre}$** and **2$_{pre}$**, on the 16 pole, 2 T wiggler beamline 9-3 at the Stanford Synchrotron Radiation Lightsource (SSRL) under standard ring conditions of 3 GeV and 100 mA ring current. A Si(220) double-crystal monochromator was used for energy selection. Other optical components used for the experiments were a Rh-coated harmonic rejection mirror and a cylindrical Rh-coated bent focusing mirror. Data on **1** and **2** were measured in fluorescence mode using a Canberra 30-element solid state Ge detector. Data on **1$_{pre}$** and **2$_{pre}$** were measured in transmission mode using an ionization chamber placed after the sample. Internal energy calibration was accomplished by simultaneous measurement of the absorption of a Co foil placed between two ionization chambers situated after the sample. The first inflection point of the foil spectrum was fixed at 7709.5 eV. The samples were monitored for potential signs of photoreduction throughout the course of data collection. To minimize the effect of beam damage and photoreduction, data were collected on an unexposed region of the sample cell after every 4 scans. Data presented here are 8 scan average spectra for both **1** and **2**, a 6 scan average spectra for **1$_{pre}$** and a 4 scan average spectra for **2$_{pre}$**. The data were processed by fitting a second-order polynomial to the pre-edge region and subtracting this from the entire spectrum as background. A three-region spline of orders 2, 3, and 3 was used to model the smoothly decaying post-edge region. The data were normalized in the Pyspline program[19] by subtracting the cubic spline and assigning the edge jump to 1.0 at 7730 eV.

Theoretical EXAFS signals $\chi(k)$ were calculated by using *FEFF* (macintosh version 8.4)[20-22] and the crystal structure of **1**, **1$_{pre}$** and **2$_{pre}$** and a structural model of **2** based on the DFT geometry optimized structure (see section 2.3). The theoretical models were fit to the data using EXAFSPAK.[23] The structural parameters varied during the fitting process were the bond distance (R) and the bond variance σ^2, which is related to the Debye-Waller factor resulting from thermal motion, and pair-wise static disorder of the absorbing and scattering atoms. The non-structural parameter E_0 (the energy at which $k = 0$) was also allowed to vary but was restricted to a common value for every component in a given fit. The S_0^2 value was set at 0.8 for the entire course of the fit. Coordination numbers were systematically varied in the course of the fit but were fixed within a given fit.

2.3 Electronic Structure Calculations

Gradient-corrected, (GGA) spin-unrestricted, broken-symmetry, density functional calculations were carried out using the ORCA[24],[25] package on an 8-cpu linux cluster. The Becke88[26],[27] exchange and Perdew86[28] correlation non-local functionals were employed to compare the electronic and geometric structure differences between **1** and **2**. The coordinates obtained from the crystal structure of **1** were used as the starting input structure for **1**. For **2**, the crystal structure of a monomeric [Co(14-TMC)(acac)]$^{3+}$ species[29] was modified to a [Co(14-TMC)O$_2$]$^+$ starting input structure. The core properties basis set CP(PPP) (as implemented in ORCA)[24],[30] was used on Co and the Ahlrichs' all electron triple-ζ TZVP[31],[32] basis set was used on all other atoms. A tight convergence criterion was selected. Population analyses were performed by means of Mulliken Population Analysis (MPA).

Wave functions were visualized and orbital contour plots were generated in Molden.[33] Compositions of molecular orbitals and overlap populations between molecular fragments were calculated using the QMForge.[19]

3 Results and Analysis

3.1 Co K-edge X-ray Absorption Spectroscopy

The normalized Co K-edge XAS spectra of **1** and **1$_{pre}$** are shown in Figure 1(A). The inset shows the expanded pre-edge region. The pre-edge feature occurs due to a quadrupole-allowed, dipole-forbidden Co 1s→3d transition and is a measure of the ligand field strength at the metal center.[34]-[36] As seen from Figure 1, on going from **1$_{pre}$** to **1**, the pre-edge energy position shifts from 7709.2 eV to 7710.1 eV indicating an increase in the ligand field strength in **1**. The edge region (∼7715 – 7725 eV) occurs due to the dipole-allowed Co 1s→4p+continuum transition and relative shifts in the edge energy position reflect the change in charge at the Co center (Q_{Co}). Furthermore, additional transitions in the rising edge can occur due to charge transfer shakeup processes or multiple scattering effects.[37]-[40] In **1**, the edge energy shifts up by ∼1.3 eV (relative to **1$_{pre}$**) to 7720.6, indicating an increase in Q_{Co}. This comparison of the Co K-edge XAS data of **1** with its Co(II) precursor **1$_{pre}$** indicates that **1** is one electron oxidized Co(III) species with an increased ligand field strength. The edge-shift combined with rR data,[17] which show an O-O stretching frequency of 902 cm^{-1} in **1**, indicate a Co(III)-peroxide electronic structure with the peroxide bound in a side-on fashion to the Co(III). The crystal structure of **1** reveals a six coordinate active site in contrast to the 5-coordinate site in **1$_{pre}$**. The higher coordination number in **1** leads to an increased ligand field strength and is consistent with the ∼0.9 eV pre-edge shift to higher energy.[41]

The normalized Co K-edge XAS spectra of **2** and **2$_{pre}$** are shown in Figure 1(B). The inset shows the expanded pre-edge region. A similar trend is observed on going from **2$_{pre}$** to **2** as observed on going from **1$_{pre}$** to **1**; the pre-edge energy position shifts from 7709.3 to 7710.1 eV, indicating an increase in the ligand field strength in **2**. The edge position shifts up from 7719.1 eV in **2$_{pre}$** to 7720.4 eV in **2**, indicating an increase in Q_{Co} on **2**. This increase in the edge energy position indicates that **2** is one electron oxidized species relative to **2$_{pre}$** and is also best described as a Co(III) complex.

3.2 Co K-edge EXAFS

Figure 2(A) shows a comparison of the non-phase shift corrected Fourier Transforms for **1** and **2**. The inset shows the EXAFS comparison. The EXAFS analysis of **1** has been published elsewhere[17] and the best fit is reproduced in Table 1 for comparison. The comparison shows that on going from **1** to **2**, the EXAFS intensity decreases dramatically with a concomitant decrease in the first shell intensity of the Fourier Transforms. Additionally, the first shell in **2** splits and a peak is observed at 1.7 Å (non-phase shift corrected). The second shell intensity decreases almost two-fold relative to that in **1**. The best fit to the EXAFS data for **2** are shown in Figure 2(B) and Table 1. The first shell was fit with 2 Co-O components at 1.88 Å and 2 Co-N at 2.10 Å. Attempts to fit the data with 2 additional Co-N components, either at the same distance (2.10 Å) or at longer distances were unsuccessful. The second shell was fit with single and multiple scattering contributions from Co-C (2.9 Å) and the corresponding Co-C-N (3.15 Å) shells. A third shell was required to fit the data with Co-C (3.5 Å) and Co-C-N (3.6 Å) shells. The presence of only 2 short Co-N distances and requirement of third shell single and multiple scattering components indicate the elongation of 2 Co-N bond to significantly longer distances in **2** such that the single scattering component is not required but the combined single and multiple scattering from the ring carbons, which is stronger, is required in the best fit. Thus, the EXAFS data

reveal that the 14-TMC ring of **2** has undergone significant distortion with two elongated Co-N distances (evidenced by the presence of long distance multiple scattering), two short Co-N distances and two shorter Co-O distances. In contrast, the EXAFS data and the crystal structure of **1** reveal that the active site has two short Co-O bonds (~1.88 Å) and four similar Co-N bonds (~ 2.0 Å).

3.3 DFT Calculations

3.3.1 [(12-TMC)CoO$_2$]$^+$—Spin unrestricted DFT calculations were performed on the [(12-TMC)CoO$_2$]$^+$ moiety obtained from the crystal structure of **1**. [(12-TMC)CoO$_2$]$^+$ can potentially exist in 14 different geometric and electronic configurations: either end-on or side-on binding mode for O$_2$ in combination with S = 0, S = 1 or S = 2 spin states at the cobalt center and S = 1/2 or S = 0 on the O$_2$.[42] Geometry optimizations were performed allowing for the calculations to converge to all 14 configurations out of which, six different electronic configurations were achieved. These six configurations were compared to investigate differences in bonding and energies. The energies and structural parameters are given in Table 2. The calculations show that the side-on bound S$_{Total}$ = 0, [(12-TMC)Co(III)O$_2^{2-}$]$^+$ electronic structure corresponds to the lowest energy configuration for **1** and is significantly more stable than any other configuration. The DFT calculated geometric and electronic structure of **1** is consistent with the x-ray diffraction, Co K-edge XAS and rR data which are consistent with a Co(III)O$_2^{2-}$ species. The ^{1}H NMR spectrum of **1** does not show paramagnetic shift over a range from -100 to 300 ppm, which indicates a S$_{Total}$ = 0 in **1**, also consistent with the DFT results. It is of interest to note that all the end-on O$_2$ bound species converge to the Co(II)-O$_2^-$ electronic configuration and so does the high-spin side-on O$_2$ bound species. Only the low-spin S$_{Total}$ = 0, side-on bound species has a Co(III)-O$_2^{2-}$ ground state, consistent with the optical and x-ray spectroscopy data.[43]

3.3.2 [(14-TMC)CoO$_2$]$^+$—Spin unrestricted DFT calculations were performed on a [(14-TMC)CoO$_2$]$^+$ moiety, which was obtained by modifying the crystal structure of the [(14-TMC)Co(acac)]$^{3+}$ complex. Similar to the [(12-TMC)CoO$_2$]$^+$ calculations above, six ground state configurations were achieved for [(14-TMC)CoO$_2$]$^+$ with a combination of starting end-on and side-on bound geometries with spin-states of S = 0, 1 and 2. The energies and structural parameters of these six configurations are shown in Table 3. In contrast to the [(12-TMC)CoO$_2$]$^+$ calculations, in which the side-on bound S$_{Total}$ = 0 was significantly more stable than any other species, the energies of the six [(14-TMC)CoO$_2$]$^+$ species differ by at most ~6 kcal/mol. Thus, the energies cannot be used to distinguish between the different electronic configurations in [(14-TMC)CoO$_2$]$^+$.

The paramagnetic shift observed in the ^{1}H NMR spectrum of **2** is consistent with an S = 1 ground state (see supporting information).[44] Based on the NMR data, either the end-on or side-on bound S$_{Total}$ = 1 species corresponds to the true ground state of **2**. DFT calculations show that the end-on bound S$_{Total}$ = 1 species converges to a Co(II)(S=1/2)-O$_2$(S=1/2) (ferromagnetically coupled) ground state, while the side-on bound S$_{Total}$ = 1 species converges to a Co(III)(S=1)-O$_2$(S=0) ground state. The XAS data presented in Figure 1 clearly show that **2** is a Co(III) species and thus confirm that the correct ground state is Co(III)(S=1)-O$_2$(S=0).[45]

The optimized geometry for **2** in the side-on bound Co(III)(S=1)-O$_2$(S=0) form has 2 Co-O bonds at 1.88 Å, 2 Co-N bonds at 2.15 Å and 2 elongated Co-N bonds at 2.31 Å, indicating a significant distortion in the 14-TMC ring. This distortion is consistent with the EXAFS analysis (Section 3.2 and Scheme 2). Note that the significant elongation of the two Co-N bonds in **2** (2.3 Å is still a bond) is consistent with a distribution of the ligand field at the Co center. This ligand field distribution leads to the stabilization of the intermediate Co(III) S =

1 species. In contrast, most six-coordinate Co(III) complexes have an (S = 0 or 2) ground state.

4 Discussion

4.1 Electronic Structure of [Co(12-TMC)O$_2$]$^+$ and [(Co(14-TMC)O$_2$]$^+$

1 and **2** are mononuclear O$_2$ bound Co complexes formed by the addition of excess H$_2$O$_2$ to their starting Co(II) analogues, **1$_{pre}$** and **2$_{pre}$**, respectively, in the presence of base. Understanding the geometric and electronic structures of **1** and **2** is an important step in our overall understanding of the M-O$_2$ bonding at biological metal centers. In this study, the geometric and electronic structures of **1** and **2** have been investigated using Co K-edge and EXAFS techniques coupled with DFT calculations. Comparison of the Co K-edge XAS edge of **1** and **2** to **1$_{pre}$** and **2$_{pre}$**, respectively, show that both **1** and **2** are Co(III) complexes. NMR data show that **1** is diamagnetic, while **2** is paramagnetic with S = 1. Together, these data reveal that the electronic structure of **1** and **2** have Co(III)(S=0)-O$_2{}^{2-}$(S=0) and Co(III) (S=1)-O$_2{}^{2-}$(S=0) ground states, respectively. EXAFS analyses of **1** and **2**, coupled with the crystal structure of **1**, demonstrates that both are side-on bound Co(III)-O$_2{}^{2-}$ species. The experimental data coupled with DFT calculations show that the 4 Co-N bonds in **1** are equidistant at ~2.0 Å from the Co center. In contrast, **2** has a distorted ligand environment with two Co-N bonds at 2.10 Å, and two elongated Co-N distances (not observed in EXAFS). DFT calculations show that these two Co-N bonds are at ~2.31 Å and are *trans* to each other. This alleviates the steric hindrance posed by the methyl groups and allows for the side-on binding of the O$_2$ group. Therefore, the 14-TMC ring in **2** undergoes significant distortion to accommodate the O$_2{}^{2-}$ to bind in a side-on fashion, which leads to a decrease in ligand field strength at the Co center and stabilizes its intermediate spin S = 1 ground state.

4.2 Correlations between NiO$_2$ and CoO$_2$ Complexes

An interesting contrast is observed between the O$_2$ bound cobalt and nickel complexes of 12-TMC and 14-TMC. Both [(12-TMC)CoO$_2$]$^+$ (**1**) and [(12-TMC)NiO$_2$]$^+$ have a side-on O$_2$ bound low-spin M(III)-O$_2{}^{2-}$ (M=Co, Ni) ground state. However, while [(14-TMC)CoO$_2$]$^+$ (**2**) has a side-on O$_2$ bound S=1 Co(III)(S=1)-O$_2{}^{2-}$(S=0) ground state, [(14-TMC)NiO$_2$]$^+$ has an end-on O$_2$ bound S=1/2 Ni(II)(S=1)-O$_2{}^-$(S=1/2) ground state. This difference is best seen in the comparison of the Ni and Co K-edge XAS data of the four complexes as shown in Figure 3. On going from [(12-TMC)NiO$_2$]$^+$ to [(14-TMC)NiO$_2$]$^+$ (Figure 3B), the edge shifts down by 1.8 eV, clearly indicating a dramatic decrease in charge in [(14-TMC)NiO$_2$]$^+$ (i.e, Ni(III) to Ni(II)).[46] In addition, Ni K-edge EXAFS analysis revealed that in contrast to [(12-TMC)NiO$_2$]$^+$, which has 2 short Ni-O bonds, [(14-TMC)NiO$_2$]$^+$ has one Ni-O bond. DFT calculations have suggested that the 14-TMC ligand with the 4 *cis*-methyl groups[47] posed a strong steric hindrance to the binding of the O$_2$ in a side-on fashion and only allowed for a relatively hindrance free end-on binding mode with a Ni(II)-O$_2{}^-$ electronic configuration. In contrast, in the 12-TMC case, the omission of two ring carbons constrained the ring, leading to an open conformation. This allowed the facile side-on binding of the O$_2$ forming a Ni(III)-O$_2{}^{2-}$ species. In contrast to the nickel systems, the similarity in the Co K-edge edge energies for **1** and **2** (Figure 3A) shows that both are Co(III) species and the EXAFS data show that both have side-on bound Co(III)-O$_2{}^{2-}$ structures. Thus, despite the steric hindrance posed by the 14-TMC ring, the O$_2$ assumes a side-on binding mode to Co in **2** and to relieve the steric constraints, the 14-TMC ring distorts as observed by experiment and DFT calculations (see section 3.2).

To understand this difference in bonding of O$_2$ to Co and Ni in the 14-TMC case, the energy contributions of the different factors that drive side-on versus end-on bonding were evaluated. The conversion of an end-on bound M^{n+}-O$_2{}^-$ to side-on bound M$^{(n+1)+}$-O$_2{}^{2-}$ is

affected by different energy terms resulting from a) the oxidation of M^{n+}, b) the reduction of O_2^-, c) potential change in exchange stabilization between the M^{n+} and O_2^- spin systems, d) differences in bonding, and e) destabilization due to steric factors. The differences in these energy terms were estimated for the O_2^{n-} bound Ni and Co complexes of 14-TMC. To evaluate factor a), DFT geometry optimizations were performed on end-on bound [(14-TMC)Ni(II)O_2^-]$^+$ and [(14-TMC)Co(II)O_2^-]$^+$ and the vertical energy changes upon oxidation of these Ni(II) and Co(II) species were calculated.[48] The calculations show that the oxidation of the Co(II) species is 11.5 kcal/mol more favorable relative to the Ni(II) species. The relative contribution of factor b) is similar in both the Co and Ni case and can be omitted from consideration. The calculated exchange stabilization in [(14-TMC)Ni(II)O_2^-]$^+$ is higher than that in [(14-TMC)Co(II)O_2^-]$^+$ by 1.8 kcal/mol.[49] On going from an end-on to a side-on binding mode of O_2, both the Co and Ni species gain an additional metal-O bond. A comparison of the Mulliken populations of the valence metal orbitals involved in bonding with the O_2^{2-} shows only minor *relative* changes on going from the Ni to the Co complex (see Supporting Information) and can also be omitted from consideration. Thus, the Co species prefers to be in the side-on $M(III)-O_2^{2-}$ configuration by $\sim$13.3 kcal/mol relative to the Ni species. The significant stability of the Co(III) oxidation state relative to the Ni(III) oxidation state overcomes the steric hindrance posed by the 4 *cis*-methyl groups in [(14-TMC)CoO_2]$^+$ leading to a distorted 14-TMC ring and a side-on O_2 bound Co(III) complex. This difference can be clearly seen in the comparison of the Fourier transforms of the EXAFS data of the Ni/Co, 12- and 14-TMC complexes (Figure 4). The first shell intensity of the two 12-TMC complexes are very similar, while a decrease in intensity is seen on going from [(14-TMC)NiO_2]$^+$ to [(14-TMC)CoO_2]$^+$, indicating the overall decrease in first shell coordination due to the weakening of two Co-N bonds.

In contrast to the 14-TMC systems with steric interactions between the 4 *cis*-methyl groups, in the steric-free [(12-TMC)NiO_2]$^+$ case, the side-on bound $Ni(III)O_2^{2-}$ form is 8.7 kcal/mol more stable than the end-on O_2 bound $Ni(II)O_2^-$ form. Combining this with the calculated relative stability of the Co(III) case, the steric constraints posed by the 14-TMC ring can be bracketed, as higher than $\sim$8.7 kcal/mol but less than $\sim$22 kcal/mol.

In summary, for both the [CoO_2]$^+$ and [NiO_2]$^+$ systems, end-on O_2 binding leads to the stabilization of an [M(II)-O_2^-]$^+$ electronic structure, while side-on O_2 binding leads to the formation of a [M(III)-O_2^{2-}]$^+$ species. The sterics of the *cis*-14-TMC chelate contributes to the geometry of O_2 binding and therefore the electronic structure for the [Ni(14-TMC)O_2]$^+$ complex results in an end-on bound $Ni(II)-O_2^-$ complex. However, the higher thermodynamic driving force for the oxidation of the Co(II) overcomes this steric constraint, resulting in the stabilization of a side-on bound $Co(III)-O_2^{2-}$ electronic structure in the 14-TMC complex.

Supplementary Material

Refer to Web version on PubMed Central for supplementary material.

Acknowledgments

References

1. Solomon EI, Sarangi R, Woertink JS, Augustine AJ, Yoon J, Ghosh S. Acc Chem Res. 2007; 40:581–591. [PubMed: 17472331]
2. Solomon EI, Brunold TC, Davis MI, Kemsley JN, Lee SK, Lehnert N, Neese F, Skulan AJ, Yang YS, Zhou J. Chem Rev. 2000; 100:235–350. [PubMed: 11749238]
3. Kovaleva EG, Lipscomb JD. Nat Chem Biol. 2008; 4:186–193. [PubMed: 18277980]
4. Hersleth HP, Ryde U, Rydberg P, Gorbitz CH, Andersson KK. J Inorg Biochem. 2006; 100:460–476. [PubMed: 16510192]
5. Costas M, Mehn MP, Jensen MP, Que L Jr. Chem Rev. 2004; 104:939–986. [PubMed: 14871146]
6. Lewis EA, Tolman WB. Chem Rev. 2004; 104:1047–1076. [PubMed: 14871149]
7. Nam W. Acc Chem Res. 2007; 40:522–531. [PubMed: 17469792]
8. Hatcher LQ, Karlin KD. J Biol Inorg Chem. 2004; 9:669–683. [PubMed: 15311336]
9. Kieber-Emmons MT, Annaraj J, Seo MS, Van Heuvelen KM, Tosha T, Kitagawa T, Brunold TC, Nam W, Riordan CG. J Am Chem Soc. 2006; 128:14230–14231. [PubMed: 17076476]
10. Cho J, Woo J, Nam W. J Am Chem Soc. 2010; 132:5958–5959. [PubMed: 20392047]
11. Cho J, Sarangi R, Annaraj J, Kim SY, Kubo M, Ogura T, Solomon EI, Nam W. Nat Chem. 2009; 1:568–572. [PubMed: 20711413]
12. Annaraj J, Suh Y, Seo MS, Kim SO, Nam W. Chem Commun (Camb). 2005:4529–4531. [PubMed: 16158103]
13. Seo MS, Kim JY, Annaraj J, Kim Y, Lee YM, Kim SJ, Kim J, Nam W. Angew Chem Int Ed. 2007; 46:377–380.
14. Hikichi S, Akita M, Moro-Oka Y. Coord Chem Rev. 2000; 198:61–87.
15. Degtyarenko I, Nieminen RM, Rovira C. Biophys J. 2006; 91:2024–2034. [PubMed: 16751243]
16. Norman, JA.; Pez, GP.; Roberts, DA. Oxygen Complexes and Oxygen Activation by Transition Metals. Martell, AE.; Sawyer, DT., editors. Plenum Press; New York: 1988.
17. Cho, J.; Sarangi, R.; Kang, H. Y.; Lee, J. Y.; Kubo, M.; Ogura, T.; Solomon, E. I.; Nam, W. **2010**, *submitted*.
18. Jo Y, Annaraj J, Seo MS, Lee YM, Kim SY, Cho J, Nam W. J Inorg Biochem. 2008; 102:2155–2159. [PubMed: 18842302]
19. Tenderholt A. Pyspline and QMForge. 2007
20. Rehr JJ, Mustre de Leon J, Zabinsky SI, Albers RC. J Am Chem Soc. 1991; 113:5135–5140.
21. Rehr JJ, Albers RC. Red Mod Phys. 2000; 72:621–654.
22. Mustre de Leon J, Rehr JJ, Zabinsky SI, Albers RC. Phys Rev B. 1991; 44:4146–4156.
23. George GN. EXAFSPAK and EDG-FIT. 2000
24. Neese F, Olbrich G. Chem Phys Lett. 2002; 362:170–178.
25. Neese F. ORCA: an ab initio, DFT and semiempirical Electronic Structure Package, Version 2.4, Revision 16. 2004
26. Becke AD. J Chem Phys. 1993; 98:5648–5652.
27. Becke AD. Phys Rev A. 1988; 38:3098–3100. [PubMed: 9900728]
28. Perdew JP. Phys Rev B. 1986; 33:8822–8824.
29. Simon E, L'Haridon P, Pichon R, L'Her M. Inorg Chim Acta. 1998; 282:173–179.
30. Sinnecker S, Slep LD, Bill E, Neese F. Inorg Chem. 2005; 44:2245–2254. [PubMed: 15792459]
31. Schaefer A, Huber C, Ahlrichs R. J Chem Phys. 1994; 100:5829–5835.
32. Schaefer A, Horn H, Ahlrichs R. J Chem Phys. 1992; 97:2571–2577.
33. Schaftenaar G, Noordik JH. J Comput Aided Mol Des. 2000; 14:123–134. [PubMed: 10721501]
34. Westre TE, Kennepohl P, DeWitt JG, Hedman B, Hodgson KO, Solomon EI. J Am Chem Soc. 1997; 119:6297–6314.
35. Penner-Hahn JE, Scott RA, Hodgson KO, Doniach S, Desjardins SR, Solomon EI. Chem Phys Lett. 1982; 88:595–598.

36. Shulman RG, Yafet Y, Eisenberger P, Blumberg WE. Proc Natl Acad Sci. 1976; 73:1384–1388. [PubMed: 5720]

37. Kosugi N, Yokoyama T, Asakura K, Kuroda H. Chem Phys. 1984; 91:249–256.

38. Frank P, Benfatto M, Hedman B, Hodgson KO. Inorg Chem. 2008; 47:4126–39. [PubMed: 18426203]

39. Bair RA, Goddard WA. Phys Rev B. 1980; 22:2767–2776.

40. An edge transition is observed at 7714.9 eV in 3 and at 7116.2 eV in 4, which can be attributed to multiple scattering contributions from the linear MeCN group.

41. Sarangi R, Aboelella N, Fujisawa K, Tolman WB, Hedman B, Hodgson KO, Solomon EI. J Am Chem Soc. 2006; 128:8286–8296. [PubMed: 16787093]

42. The configurations are the side-on and end-on bound forms of: $CoII(S=3/2)+O_2^-(S=1/2)$, $CoIII(S=2)+O_2^{2-}(S=0)$, $CoIII(S=1)+O_2^-(S=0)$, $CoII(S=1/2)+O_2^-(S=1/2)$, $CoII(S=3/2)+O_2^-(S=-1/2)$, $CoIII(S=0)+O_2^{2-}(S=0)$, $CoII(S=1/2)+O_2^-(S=-1/2)$.

43. The bond distances and Mulliken spin densities on the intermediate spin $S_{Total}=1$ species indicate a mixed $Co(III)-O_2^{2-}/Co(II)-O_2^-$ character in the ground state.

44. Note that in an earlier publication 2 was assigned a S=2 ground state based on the observation of paramagnetic NMR data.[17] Recent NMR data indicate that the previous assignment was erroneous owing to the presence of extraneous contamination.

45. Note that the calculated energy of $Co(III)(S=1)-O_2(S=0)$ is higher than the $Co(III)(S=0)-O_2(S=0)$ species by 4.6 Kcal/mol. However, the NMR data clearly show that 2 is paramagnetic, excluding the possibility that 2 is $Co(III)(S=2)-O_2(S=0)$.

46. Sarangi R, Dey M, Ragsdale SW. Biochemistry. 2009; 48:3146–56. [PubMed: 19243132]

47. FEFF fits to the EXAFS data were consistent with all four methyl groups cis to the O_2 binding side.

48. The calculations were performed in the appropriate spin states and were checked to confirm that the vertical oxidation only affected the metal center.

49. The exchange stabilization energy was obtained from the optimized energies of the high-spin and low-spin states of $[(14-TMC)Ni(II)O^{2-}]^+$ and $[(14-TMC)Co(II)O^{2-}]^+$.[50,51]

50. Noodleman L. J Chem Phys. 1981; 74:5737–5743.

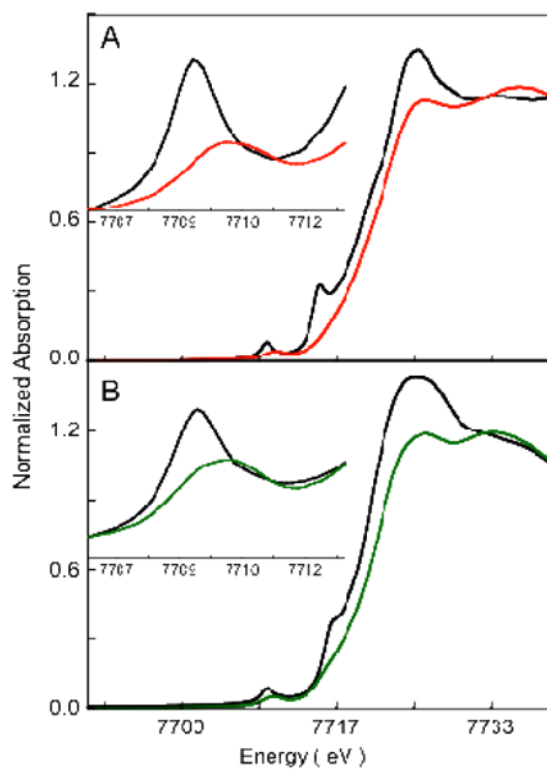51. Noodleman L, Davidson ER. Chem Phys. 1985; 109:131–138.

Figure 1.
Normalized Co K-edge XAS spectra. A: **1** (——) and **1$_{pre}$** (——); B: **2** (——) and **2$_{pre}$** (——). The insets show the expanded pre-edge region.
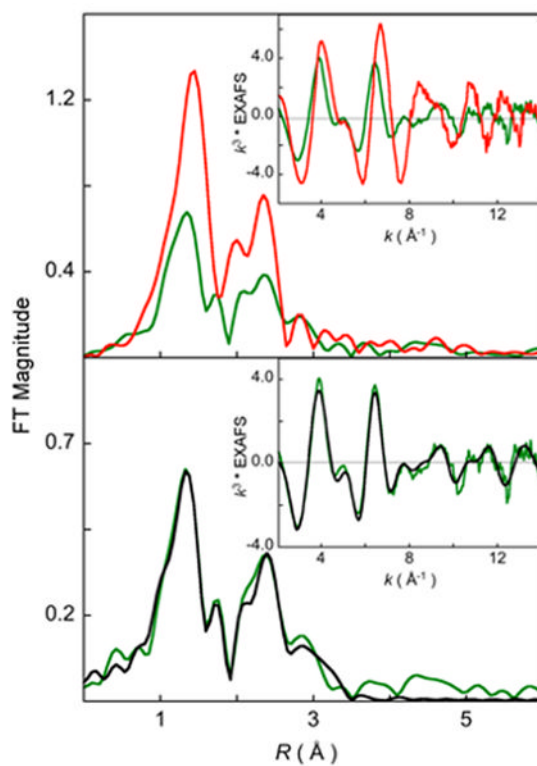
Figure 2.
(A) Comparison of the non-phase shift corrected Fourier Transforms for **1** (────) and **2** (────). The inset shows the EXAFS comparison. (B) *FEFF* best fit results for **2**. Data (────) and fit (────).
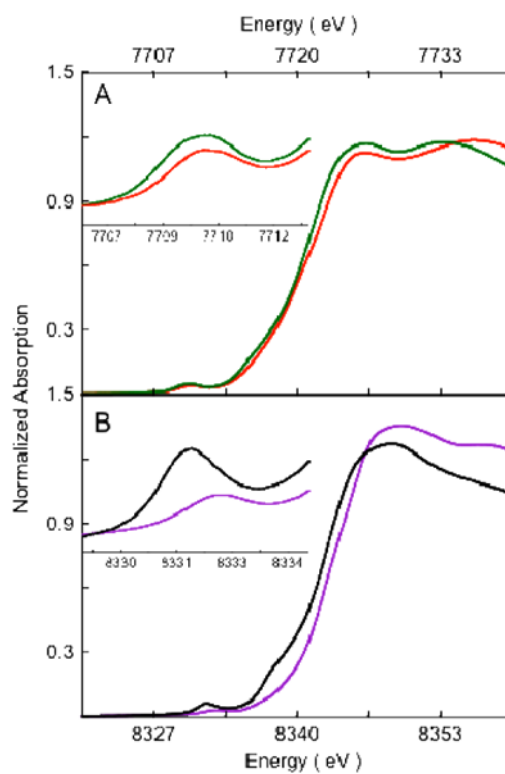
Figure 3.
Comparison of the XAS pre-edge and edge shifts. (A): Co K-edge for **1** (———) and **2** (———). (B): Ni K-edge for $[(12\text{-}TMC)NiO_2]^+$ (———) and $[(14\text{-}TMC)NiO_2]^+$ (———). Insets show the expanded pre-edge region.
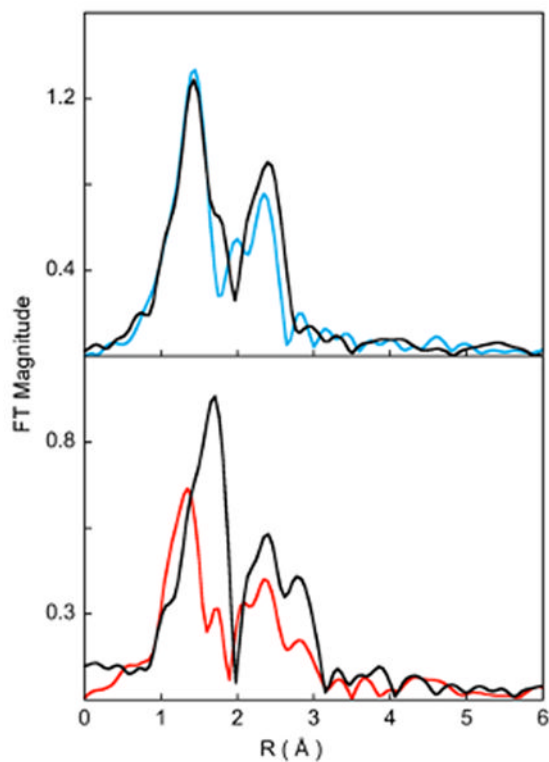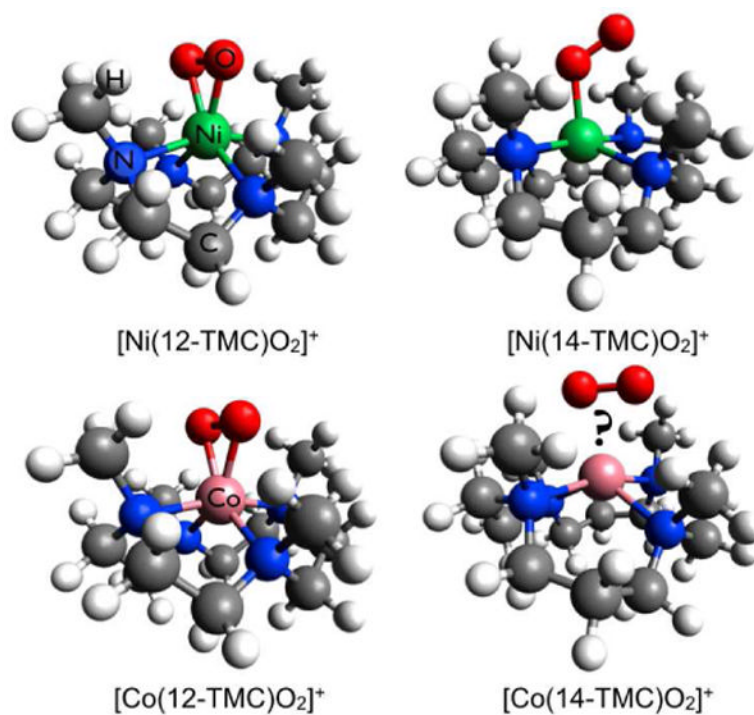
Figure 4.
Comparison of the non-phase shift corrected Fourier Transforms for A: **1** (——) and [(12-TMC)NiO$_2$](ClO$_4$) (——), B: **2** (——) and [(14-TMC)NiO$_2$](ClO$_4$) (——).

Scheme 1.
The geometric structures of [Ni(12-TMC)O$_2$]$^+$ (crystal structure), [Ni(14-TMC)O$_2$]$^+$ (obtained from a combination of spectroscopic techniques and DFT calculations) and [Co(12-TMC)O$_2$]$^+$ (crystal structure). The structure of [Co(14-TMC)O$_2$]$^+$ has not been accessible via x-ray diffraction. Color code: Ni(green), Co(pink), O(red), N(blue), C(grey) and H(white)
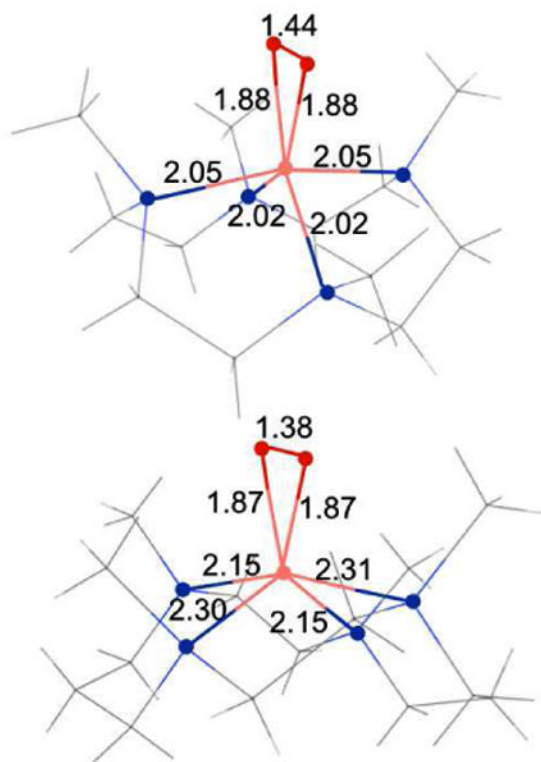
Scheme 2.
The DFT calculated nearest neighbor distances for **1** (top) and **2** (bottom).

NIH-PA Author Manuscript

NIH-PA Author Manuscript

NIH-PA Author Manuscript

Table 1

EXAFS Least Squares Fitting Results

Complex	Coordination/Path	R(Å)[a]	σ^2(Å^2)[b]	E$_0$ (eV)	F [c]
1	2 Co-O	1.85	323		
	4 Co-N	1.99	317		
	8 Co-C[d]	2.84	393	1.81	0.16
	24 Co-C-N[d]	3.14	382		
2	2 Co-O	1.88	341		
	2 Co-N	2.10	530		
	4 Co-C[d]	2.90	853		
	8 Co-C-N[d]	3.16	853	2.91	0.08
	4 Co-C-N[e]	3.52	628		
	12 Co-C-N[e]	3.57	224		

[a]The estimated standard deviations for the distances are in the order of ± 0.02 Å.

[b]The σ^2 values are multiplied by 10^5.

[c]Error is given by $\Sigma[(\chi obsd - \chi calcd)^2 k^6]/\Sigma[(\chi obsd)^2 k^6]$.

[d]The SS and MS contribution from the carbon atoms adjacent to the two 2.10 Å N atoms.

[e]The longer distance SS and MS distances were required to fit the outer shell of the FT.

Table 2

Selected DFT Parameters for [(12-TMC)CoO$_2$]$^+$

		End-on S$_{Total}$=0	End-on S$_{Total}$=1	End-on S$_{Total}$=2	Side-on S$_{Total}$=0	Side-on S$_{Total}$=1	Side-on S$_{Total}$=2
ΔE (Kcal/mol)^a		0	-1.3	6.6	-13.6	-5.1	6.5
Structural Parameters	Co-O	1.80	1.79	2.1	1.88	1.86	2.07
	O-O	1.35	1.35	1.34	1.44	1.37	1.33
	Co-N(N')^b	2.06(2.11)	2.06(2.12)	2.14(2.20)	2.02(2.05)	2.07(2.26)	2.13(2.19)
Spin Density^b Co, O$_2$		0.6, -0.6	1.3, 0.6	2.6, 1.2	0, 0	1.6, 0.4	2.7, 1.2

^{a}The ΔE is calculated as (E-E$_{End-on}$, S(Total)=0).

^{b}The Co-N(N') distances are the average of two trans Co-N bonds.

^{b}The Mulliken spin densities for Co and O$_2$ are shown (the spin densities on both O atoms have been added to represent O$_2$).

Table 3

Selected DFT Parameters for [(14-TMC)CoO$_2$]$^+$

		End-on S$_{Total}$ = 0	End-on S$_{Total}$ = 1	End-on S$_{Total}$ = 2	Side-on S$_{Total}$ = 0	Side-on S$_{Total}$ = 1	Side-on S$_{Total}$ = 2
ΔE (Kcal/mol)[a]		0	-4.1	0.52	-5.1	-0.5	1.0
Structural Parameters	Co-O	1.85	1.84	1.87	1.90	1.87	2.03
	O-O	1.35	1.35	1.33	1.42	1.38	1.36
	Co-N(N')[b]	2.07(2.18)	2.08(2.17)	2.14(2.25)	2.08(2.13)	2.15(2.31)	2.13(2.19)
Spin Density[b] Co, O$_2$		-0.5, 0.5	1.3, 0.7	2.6, 1.1	0, 0	1.8, 0.1	2.7, 1.1

[a]The ΔE is calculated as (E-EEnd-on, S(Total)=0).

[b]The Co-N(N') distances are the average of two trans Co-N bonds.

[b]The Mulliken spin densities for Co and O$_2$ are shown (the spin densities on both O atoms have been added to represent O$_2$).